

Interpolation-free monotone finite volume method for diffusion equations on polygonal meshes

K. Lipnikov^a, D. Svyatskiy^{a,*}, Y. Vassilevski^b

^a *Mathematical Modeling and Analysis Group, Theoretical Division, Los Alamos National Laboratory, Los Alamos, NM 87545, United States*

^b *Institute of Numerical Mathematics, Russian Academy of Sciences, 8, Gubkina, 119333 Moscow, Russia*

ARTICLE INFO

Article history:

Received 8 May 2008

Received in revised form 29 August 2008

Accepted 24 September 2008

Available online 1 November 2008

Keywords:

Diffusion equation

Monotone method

Polygonal mesh

ABSTRACT

We developed a new monotone finite volume method for diffusion equations. The second-order linear methods, such as the multipoint flux approximation, mixed finite element and mimetic finite difference methods, are not monotone on strongly anisotropic meshes or for diffusion problems with strongly anisotropic coefficients. The finite volume (FV) method with linear two-point flux approximation is monotone but not even first-order accurate in these cases. The developed monotone method is based on a nonlinear two-point flux approximation. It does not require any interpolation scheme and thus differs from other nonlinear finite volume methods based on a two-point flux approximation. The second-order convergence rate is verified with numerical experiments.

Published by Elsevier Inc.

1. Introduction

Anisotropic diffusion appears in many physical models describing subsurface flows, head conduction in structured materials and crystals, biological systems, and plasma physics. Anisotropic diffusion has shown to be a powerful denoising tool in image processing [1]. Accurate modeling of diffusive processes in these applications requires reliable discretization methods. In this article we develop a new finite volume method that preserves solution positivity.

The linear methods, such as the multipoint flux approximation (MPFA), the mixed finite element (MFE) and the mimetic finite difference (MFD) methods, are second-order accurate on unstructured meshes but may produce non-monotone solutions even when the diffusion coefficient is moderately (1:100) anisotropic. The linear two-point flux approximation finite volume (FV) method, used for instance in modeling flows in porous media, is monotone but not even first-order accurate for anisotropic problems. Monotonicity of the MPFA methods is analyzed in [2,3]. The theoretical analysis of sufficient mesh conditions providing the discrete maximum principle (DPM) has been formulated in 70's by Ciarlet and Raviart [4] for piecewise-linear finite element approximations. Later, the DPM has been shown for weaker mesh conditions [5,6]. To guarantee solution positivity for general meshes, a number of nonlinear methods have been proposed for the Poisson equation [7] and more recently for general diffusion equation [8–13].

The monotone FV method proposed in this article is based on a nonlinear two-point flux approximation scheme. The original idea belongs to LePotier [8]. In [9], we proved monotonicity of his method for steady-state diffusion problems and extended it to shape-regular polygonal meshes and scalar diffusion coefficients. In three-dimensions the method has been proposed and analyzed by Kapyrin [12,13]. Further development of the method was made by Yuan and Sheng [10]. Their method can be applied to a much bigger class of polygonal meshes consisting of star-shaped cells and full tensor diffusion coefficients. The common property of all these methods is that in addition to *primary* unknowns defined at mesh cells,

* Corresponding author. Tel.: +1 505 606 2124; fax: +1 505 665 5757.

E-mail addresses: lipnikov@lanl.gov (K. Lipnikov), dasvyat@lanl.gov (D. Svyatskiy), vasilevs@dodo.inm.ras.ru (Y. Vassilevski).

solution values at mesh vertices are involved in the method construction. These *auxiliary* unknowns are interpolated from primary, cell-based unknowns. The interpolation problem becomes even a more challenging task when the diffusion coefficient is discontinuous. The interpolation methods studied in [10] use a piecewise-linear approximation to the solution around points where the coefficient is discontinuous. However, as shown in [9,10], the choice of the interpolation method affects the accuracy of the nonlinear FV method even in the case of a constant diffusion coefficient. The choice of an interpolation method depends of the problem. The particular interpolation method may be efficient for one problem and be inaccurate for another. The nonlinear FV method proposed in this article does not use any auxiliary unknowns at mesh vertices, and thus is the next step towards efficiency of nonlinear two-point flux approximation methods. It is exact for linear and piecewise-linear solutions and thus has the second-order truncation error. Our numerical experiments show the second-order convergence rate in the mesh-dependent L_2 -norm.

The two-point flux approximation methods result in schemes with a compact stencil. For square meshes and a diagonal diffusion tensor this stencil reduces to the conventional five-point stencil. The major computational overhead in nonlinear FV methods comes from the solution of a nonlinear algebraic problem. The Picard method, used in this and the other papers, guarantees that the solution is positive on each iteration. Our numerical experiments demonstrate that the proposed method requires lesser number of nonlinear iterations than the methods using interpolation algorithms.

The paper outline is as follows. In Section 2, we state the diffusion problem. In Section 3, we describe the nonlinear finite volume scheme. In Section 4, we prove monotonicity of the proposed scheme. In Section 5, we present numerical analysis of the scheme using triangular, quadrilateral and polygonal meshes.

2. Steady diffusion equation

Let Ω be a two-dimensional polygonal domain with boundary $\Gamma = \Gamma_N \cup \Gamma_D$ where $\Gamma_D = \bar{\Gamma}_D$ and $\Gamma_D \neq \emptyset$. We consider a model diffusion problem for unknown concentration c :

$$\begin{aligned} -\operatorname{div}(\mathbb{K}\nabla c) &= f \quad \text{in } \Omega, \\ c &= g_D \quad \text{on } \Gamma_D, \\ -\mathbb{K}\frac{\partial c}{\partial \mathbf{n}} &= g_N \quad \text{on } \Gamma_N, \end{aligned} \quad (1)$$

where $\mathbb{K}(\mathbf{x}) = \mathbb{K}^T(\mathbf{x}) > 0$ is an anisotropic diffusion tensor, f is a source term, and \mathbf{n} is the exterior normal vector.

Let \mathcal{T} be a conformal polygonal mesh composed from shape-regular cells. Let $N_{\mathcal{T}}$ be the number of polygonal cells and N_B be the number of boundary edges. We assume that \mathcal{T} is edge-connected, i.e. it cannot be split into two meshes having no common edges. We also assume that the tensor \mathbb{K} is constant inside each cell; however, it may jump across mesh edges as well as may change orientation of principal directions. Finally, we assume that each polygon has at most one edge across which \mathbb{K} is discontinuous. This can be always achieved by breaking some of the mesh cells into a few new cells.

We denote by $\mathcal{E}_I, \mathcal{E}_B$ disjoint sets of interior and boundary edges. The subset \mathcal{E}_J of \mathcal{E}_I collects edges with jumping diffusion tensor. The set \mathcal{E}_B is further split into subsets \mathcal{E}_B^D and \mathcal{E}_B^N where the Dirichlet and Neumann boundary conditions, respectively, are imposed. Finally, $\mathcal{E}_{\mathcal{T}}$ denotes the set of edges of polygon T .

3. Monotone nonlinear FV scheme on polygonal meshes

Let $\mathbf{q} = -\mathbb{K}\nabla c$ denote the flux which satisfies the mass balance equation:

$$\operatorname{div} \mathbf{q} = f \quad \text{in } \Omega. \quad (2)$$

In this section, we derive a FV scheme with a nonlinear two-point flux approximation. Integrating equation (2) over a polygon T and using the Green's formula we get:

$$\int_{\partial T} \mathbf{q} \cdot \mathbf{n}_T ds = \int_T f dx, \quad (3)$$

where \mathbf{n}_T denotes the outer unit normal to ∂T . Let e denote an edge of cell T and \mathbf{n}_e be the corresponding normal vector. For a single cell T , we always assume that \mathbf{n}_e is the outward normal vector. In all other cases, we specify orientation of \mathbf{n}_e . It will be convenient to assume that $|\mathbf{n}_e| = |e|$ where $|e|$ denotes the length of edge e . The equation (3) becomes

$$\sum_{e \in \partial T} \mathbf{q}_e \cdot \mathbf{n}_e = \int_T f dx, \quad (4)$$

where \mathbf{q}_e is the average flux density for edge e .

For each cell T , we assign one degree of freedom, C_T , for concentration c . Let C be the vector of all discrete concentrations. If two cells T_+ and T_- have a common edge e , the two-point flux approximation is as follows:

$$\mathbf{q}_e^h \cdot \mathbf{n}_e = M_e^+ C_{T_+} - M_e^- C_{T_-}, \quad (5)$$

where M_e^+ and M_e^- are some coefficients. In a linear FV method, these coefficients are equal and fixed. In the nonlinear FV method, they may be different and depend on concentrations in surrounding cells. On edge $e \in \Gamma_D$, the flux has a form similar

to (5) with an explicit value for one of the concentrations. For the Dirichlet boundary value problem, $\Gamma_D = \partial\Omega$, substituting (5) into (4), we obtain a system of N_T equations with N_T unknowns C_T . Dirichlet and Neumann boundary conditions are considered in Section 3.3.

3.1. Notations

For every T in \mathcal{T} , we define the barycenter \mathbf{x}_T^* and a collocation interior point \mathbf{x}_T . Similarly, for every edge $e \in \mathcal{E}_B \cup \mathcal{E}_J$, we define the barycenter \mathbf{x}_e^* and a collocation point \mathbf{x}_e . If e is the boundary edge, we set $\mathbf{x}_e = \mathbf{x}_e^*$. If the diffusion tensor is not changing across edges of T , we set $\mathbf{x}_T = \mathbf{x}_T^*$. Otherwise, the collocation point is selected according to the rules defined in Lemma 3.2.

For every T we define a set Σ_T of nearby collocation points as follows. First, we add to Σ_T the collocation point \mathbf{x}_T . Then, for every interior edge $e \in \mathcal{E}_T \setminus (\mathcal{E}_J \cup \mathcal{E}_B)$, we add the collocation point $\mathbf{x}_{T'_e}$, where T'_e is the cell, other than T , that has edge e . If $e \in \mathcal{E}_T \cap \mathcal{E}_J$, we add to Σ_T the collocation point \mathbf{x}_e . Finally, for every boundary edge $e \in \mathcal{E}_T \cap \mathcal{E}_B$, we add the collocation point \mathbf{x}_e . Let $N(\Sigma_T)$ denote the cardinality of Σ_T .

We shall refer to collocation points on edges $e \in \mathcal{E}_J \cup \mathcal{E}_B$ as the *secondary* collocation points. They are introduced for mathematical convenience and will not enter the final algebraic system. In contrast, we shall refer to the other collocation points as the *primary* collocation points.

We assume that for every $e \in \mathcal{E}_T$, there exist two points $\mathbf{x}_{e,1}$ and $\mathbf{x}_{e,2}$ in set Σ_T such that the following two conditions are hold. First, if

$$\mathbf{t}_{e,1} = \mathbf{x}_{e,1} - \mathbf{x}_T, \quad \mathbf{t}_{e,2} = \mathbf{x}_{e,2} - \mathbf{x}_T,$$

and $\theta_{e,i}$, $i = 1, 2$, is the angle between $\mathbf{t}_{e,i}$ and the co-normal vector $\ell_e = \mathbb{K}_T \mathbf{n}_e$, then

$$\theta_{e,1} < \pi, \quad \theta_{e,2} < \pi \quad \text{and} \quad \theta_{e,1} + \theta_{e,2} < \pi. \tag{6}$$

Second, the vectors $\mathbf{t}_{e,i}$ and ℓ_e satisfy

$$\mathbf{t}_{e,1} \times \ell_e \leq 0, \quad \mathbf{t}_{e,2} \times \ell_e > 0. \tag{7}$$

In simple words, the co-normal vector ℓ_e is assumed to lie between vectors $\mathbf{t}_{e,1}$ and $\mathbf{t}_{e,2}$, as shown in Fig. 1, and all angles are less than π . If conditions (6) and (7) are violated, we may add to the set Σ_T the neighbors of already included collocation points.

Lemma 3.1. Under assumptions (6) and (7), there exist positive α_e and β_e such that

$$\frac{1}{|\ell_e|} \ell_e = \frac{\alpha_e}{|\mathbf{t}_{e,1}|} \mathbf{t}_{e,1} + \frac{\beta_e}{|\mathbf{t}_{e,2}|} \mathbf{t}_{e,2}. \tag{8}$$

Moreover,

$$\alpha_e = \frac{\sin \theta_{e,2}}{\sin(\theta_{e,1} + \theta_{e,2})} \quad \text{and} \quad \beta_e = \frac{\sin \theta_{e,1}}{\sin(\theta_{e,1} + \theta_{e,2})}.$$

The proof of Lemma may be found in [10].

3.2. Nonlinear two-point flux approximation for an interior edge

Let e be an interior edge. We denote by T_+ and T_- the cells that share e and assume that \mathbf{n}_e is outward for T_+ . Let \mathbf{x}_\pm (or \mathbf{x}_{T_\pm}) and \mathbf{x}_\pm^* be the collocation point and the barycenter of T_\pm , respectively. Let $\mathbb{K}_\pm = \mathbb{K}(\mathbf{x}_\pm^*)$ and C_\pm (or C_{T_\pm}) be the discrete concentrations in T_\pm .

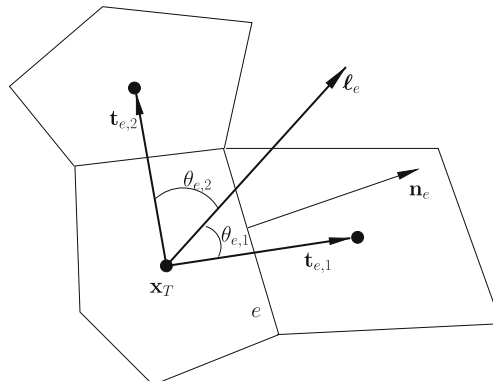


Fig. 1. Notation: vector ℓ_e forms acute angles with vectors $\mathbf{t}_{e,1}$ and $\mathbf{t}_{e,2}$; the collocation points are marked by solid circles.

We begin with the case when $\mathbb{K}_+ = \mathbb{K}_- = \mathbb{K}$. Let $T = T_+$.

Using the above notations, definition of the directional derivative

$$\frac{\partial c}{\partial \ell_e} | \ell_e | = \nabla c \cdot (\mathbb{K} \mathbf{n}_e),$$

and Lemma 3.1, we write

$$\mathbf{q}_e \cdot \mathbf{n}_e = -\frac{|\ell_e|}{|e|} \int_e \frac{\partial c}{\partial \ell_e} ds = -\frac{|\ell_e|}{|e|} \int_e \left(\alpha_e \frac{\partial c}{\partial \mathbf{t}_{e,1}} + \beta_e \frac{\partial c}{\partial \mathbf{t}_{e,2}} \right) ds. \quad (9)$$

Replacing directional derivatives by finite differences, we get

$$\int_e \frac{\partial c}{\partial \mathbf{t}_{e,i}} ds = \frac{C_{e,i} - C_T}{|\mathbf{x}_{e,i} - \mathbf{x}_T|} |e| + O(h_T^2), \quad i = 1, 2, \quad (10)$$

where h_T is the diameter of T . Note that this formula is exact for linear concentrations. If $\mathbf{x}_{e,i}$ is the secondary collocation point, we use formula (19) to replace $C_{e,i}$ by a linear combination of concentrations in primary collocation points from Σ_T . Using the finite difference approximations (10), we transform formula (9) to

$$\mathbf{q}_e^h \cdot \mathbf{n}_e = -|\ell_e| \left(\frac{\alpha_e}{|\mathbf{t}_{e,1}|} (C_{e,1} - C_T) + \frac{\beta_e}{|\mathbf{t}_{e,2}|} (C_{e,2} - C_T) \right). \quad (11)$$

At the moment, this flux involves three rather than two concentrations. To derive a two-point flux approximation, we consider polygon T_- and derive another approximation of flux through edge e . To distinguish between T_+ and T_- , we add subscripts \pm and omit subscript e . Since \mathbf{n}_e is the internal normal vector for T_- , we have to change sign of the right-hand side:

$$\mathbf{q}_\pm^h \cdot \mathbf{n}_e = \mp |\ell_e| \left(\frac{\alpha_\pm}{|\mathbf{t}_{\pm,1}|} (C_{\pm,1} - C_\pm) + \frac{\beta_\pm}{|\mathbf{t}_{\pm,2}|} (C_{\pm,2} - C_\pm) \right), \quad (12)$$

where α_\pm and β_\pm are given by Lemma 3.1 and $C_{\pm,i}$ denote concentrations at points $\mathbf{x}_{\pm,i}$ from Σ_{T_\pm} .

We define a new flux as a linear combination of $\mathbf{q}_\pm^h \cdot \mathbf{n}_e$ with non-negative weights μ_\pm :

$$\begin{aligned} \mathbf{q}_e^h \cdot \mathbf{n}_e &= \mu_+ \mathbf{q}_+^h \cdot \mathbf{n}_e - \mu_- \mathbf{q}_-^h \cdot \mathbf{n}_e \\ &= \mu_+ |\ell_e| \left(\frac{\alpha_+}{|\mathbf{t}_{+,1}|} + \frac{\beta_+}{|\mathbf{t}_{+,2}|} \right) C_+ - \mu_- |\ell_e| \left(\frac{\alpha_-}{|\mathbf{t}_{-,1}|} + \frac{\beta_-}{|\mathbf{t}_{-,2}|} \right) C_- - \mu_+ |\ell_e| \left(\frac{\alpha_+}{|\mathbf{t}_{+,1}|} C_{+,1} + \frac{\beta_+}{|\mathbf{t}_{+,2}|} C_{+,2} \right) \\ &\quad + \mu_- |\ell_e| \left(\frac{\alpha_-}{|\mathbf{t}_{-,1}|} C_{-,1} + \frac{\beta_-}{|\mathbf{t}_{-,2}|} C_{-,2} \right). \end{aligned} \quad (13)$$

The obvious requirement for the weights is to cancel the terms in the last row of (13) which results in a two-point flux formula. The second requirement is to approximate the true flux. These requirements lead us to the following system:

$$\begin{cases} -\mu_+ d_+ + \mu_- d_- = 0, \\ \mu_+ + \mu_- = 1, \end{cases} \quad (14)$$

where

$$d_\pm = |\ell_e| \left(\frac{\alpha_\pm}{|\mathbf{t}_{\pm,1}|} C_{\pm,1} + \frac{\beta_\pm}{|\mathbf{t}_{\pm,2}|} C_{\pm,2} \right). \quad (15)$$

Since coefficients d_\pm depend on both geometry and concentration, the weights μ_\pm do as well. Thus, the resulting two-point flux approximation is *nonlinear*.

Remark 3.1. Note that concentration $C_{+,i}$ (resp., $C_{-,i}$), $i = 1, 2$, may be defined at the same collocation point as C_- (resp., C_+). In this case the terms to be canceled are changed. By doing so, we recover the classical linear scheme for square meshes with the 4-1-1-1 stencil. A similar conclusion can be drawn for centroidal Voronoi meshes. To simplify the presentation, we shall not consider this and similar special cases.

The solution of (14) can be written explicitly. In all cases $d_\pm \geq 0$ if $C \geq 0$. If $d_\pm = 0$, we set $\mu_+ = \mu_- = \frac{1}{2}$. Otherwise

$$\mu_+ = \frac{d_-}{d_- + d_+} \quad \text{and} \quad \mu_- = \frac{d_+}{d_- + d_+}. \quad (16)$$

This implies that the weights μ_\pm are non-negative. Substituting this into (13), we get the two-point flux formula (5) with coefficients

$$M_e^\pm = \mu_\pm |\ell_e| (\alpha_\pm / |\mathbf{t}_{\pm,1}| + \beta_\pm / |\mathbf{t}_{\pm,2}|). \quad (17)$$

Now we consider the case when $\mathbb{K}_+ \neq \mathbb{K}_-$. In this case, the collocation points \mathbf{x}_\pm depend on both tensors. Let $\ell_\pm = \mp \mathbb{K}_\pm \mathbf{n}_e$ be two co-normal vectors to edge e outward with respect to T_\pm .

Lemma 3.2. *For every edge $e \in \mathcal{E}_j$ shared by polygons T_+ and T_- , there exist two primary collocation points \mathbf{x}_+ and \mathbf{x}_- and one secondary collocation point \mathbf{x}_e such that*

$$(\mathbf{x}_e - \mathbf{x}_+) \times \ell_+ = 0 \quad \text{and} \quad (\mathbf{x}_e - \mathbf{x}_-) \times \ell_- = 0.$$

The proof is based on the fact that the line defined by vector ℓ_\pm and passing through any interior point of e has a non-empty intersection with interior of T_\pm . In the computer program we choose collocation points \mathbf{x}_\pm that satisfy the lemma condition and minimize the following functional:

$$\Phi(\mathbf{x}_+, \mathbf{x}_-) = \frac{|\mathbf{x}_+ - \mathbf{x}_+^*|^2}{|T_+|} + \frac{|\mathbf{x}_- - \mathbf{x}_-^*|^2}{|T_-|}.$$

The consequence of Lemma 3.2 is that formulae (12) are reduced to a two-point flux approximation:

$$\mathbf{q}_\pm^h \cdot \mathbf{n}_e = \mp \frac{|\ell_\pm|}{|\mathbf{x}_e - \mathbf{x}_\pm|} (C_e - C_\pm). \tag{18}$$

Continuity of the flux at edge e gives a linear relation for concentration C_e

$$(C_e - C_+) |\ell_+| |\mathbf{x}_e - \mathbf{x}_-| + (C_e - C_-) |\ell_-| |\mathbf{x}_e - \mathbf{x}_+| = 0. \tag{19}$$

Calculating C_e from (19) and substituting it in (18), we obtain

$$\mathbf{q}_+^h \cdot \mathbf{n}_e = -\mathbf{q}_-^h \cdot \mathbf{n}_e = \frac{|\ell_+| |\ell_-|}{|\ell_+| |\mathbf{x}_e - \mathbf{x}_-| + |\ell_-| |\mathbf{x}_e - \mathbf{x}_+|} (C_+ - C_-).$$

Thus, the non-negative coefficients in (5) are equal

$$M_e^+ = M_e^- = \frac{|\ell_+| |\ell_-|}{|\ell_+| |\mathbf{x}_e - \mathbf{x}_-| + |\ell_-| |\mathbf{x}_e - \mathbf{x}_+|}. \tag{20}$$

3.3. Neumann and Dirichlet boundary conditions

First, we consider the case of Neumann boundary edge $e \in \mathcal{E}_B^N$. The flux through this edge is

$$\mathbf{q}_e^h \cdot \mathbf{n}_e = \bar{g}_{N,e} |e|, \tag{21}$$

where $\bar{g}_{N,e}$ is the mean value of g_N on edge e . Despite that this flux is given, there may be fluxes (13) using concentration C_e . Thus an equation for concentration C_e is needed. It is derived following the argument in the beginning of Section 3.2. It may be convenient to think about e as the cell with zero area. Let T be the cell with edge e . Replacing C_+ and C_- with C_T and C_e , respectively, we get

$$\mathbf{q}_e^h \cdot \mathbf{n}_e = M_e^+ C_T - M_e^- C_e, \tag{22}$$

where coefficients M_e^\pm are given by (17). The required equation is then

$$M_e^- C_e - M_e^+ C_T = -\bar{g}_{N,e} |e|. \tag{23}$$

Now consider the case of the Dirichlet boundary edge $e \in \mathcal{E}_B^D$. Let T be again the cell with this edge. The equation for concentration is trivial

$$C_e = \bar{g}_{D,e} = \frac{1}{|e|} \int_e g_D ds. \tag{24}$$

The equation for the flux is given by (22).

4. Discrete system and monotonicity analysis

For every T in \mathcal{T} , the cell equation (4) is

$$\sum_{e \in \mathcal{E}_T} \chi(T, e) \mathbf{q}_e^h \cdot \mathbf{n}_e = \int_T f dx, \tag{25}$$

where $\chi(T, e)$ is either 1 or -1 depending on mutual orientation of normal vectors \mathbf{n}_e and \mathbf{n}_T . Substituting two-point flux formula (5) with non-negative coefficients given by (17) and (20) into (25), and using equations (23) and (24) to eliminate boundary concentrations, we get a nonlinear system of N_T equations

$$\mathbb{M}(C)C = F(C). \quad (26)$$

The matrix $\mathbb{M}(C)$ may be represented by assembling of 2×2 matrices

$$\mathbb{M}_e(C) = \begin{pmatrix} M_e^+(C) & -M_e^-(C) \\ -M_e^+(C) & M_e^-(C) \end{pmatrix} \quad (27)$$

for the interior edges and 1×1 matrices $\mathbb{M}_e(C) = M_e^+(C)$ for Dirichlet edges (see Algorithm 1 for more detail). The right-hand side vector $F(C)$ is generated by the source and the boundary data:

$$F_T(C) = \int_T f dx + \sum_{e \in \mathcal{E}_B^D \cap \partial T} M_e^-(C) \bar{g}_{D,e} - \sum_{e \in \mathcal{E}_B^N \cap \partial T} |e| \bar{g}_{N,e}, \quad \forall T \in \mathcal{T}, \quad (28)$$

for $f(x) \geq 0$, $g_D \geq 0$ and $g_N \leq 0$ the components of vector F are non-negative. We use the Picard iterations to solve the nonlinear system (26) (see Algorithm 1).

Algorithm 1: Generation and solution of nonlinear system (26)

- 1: Calculate primary and secondary collocation points (first paragraph in Section 3.1 and Lemma 3.1).
- 2: For each interior edge $e \in \mathcal{E}_I \setminus \mathcal{E}_J$ shared by elements T_\pm find vectors $\mathbf{t}_{\pm,1}$, $\mathbf{t}_{\pm,2}$ satisfying conditions (6) and (7). Find similar vectors for Neumann boundary edges.
- 3: Select an initial vector C^0 with non-negative entries and a small value $\varepsilon_{non} > 0$.
- 4: **for** $k = 0, \dots, \mathbf{do}$
- 5: Assemble the global matrix $\mathbb{M}(C^k)$ from the edge-based matrices $\mathbb{M}_e(C^k)$. If $e \in \mathcal{E}_J$, use formula (20) to form $\mathbb{M}_e(C^k)$. For the other edges use (17) with (15) and (16).
- 6: Calculate the right-hand side vector $F(C^k)$ using (28).
- 7: Solve $\mathbb{M}(C^k)C^{k+1} = F(C^k)$.
- 8: Calculate concentrations C_e at the secondary collocation points on edges $e \in \mathcal{E}_J \cup \mathcal{E}_B$ using (19), (23) and (24).
- 9: Stop if $\|\mathbb{M}(C^{k+1})C^{k+1} - F(C^{k+1})\| \leq \varepsilon_{non} \|\mathbb{M}(C^0)C^0 - F(C^0)\|$.
- 10: **end for**

The linear system in Step 7 with the non-symmetric matrix $\mathbb{M}(C^k)$ is solved by the bi-conjugate gradient stabilized (BiCG-Stab) method [14] with the second-order ILU preconditioner [15]. The BiCGStab iterations are terminated when the relative norm of the initial residual $\mathbb{M}(C^k)C^k - F(C^k)$ becomes smaller than ε_{lin} .

Let us show that the matrix $\mathbb{M}(C^k)$ is the M -matrix provided that $C^k > 0$. Our derivation shows that coefficients $M_e^\pm(C^k)$ are positive. Thus, all diagonal entries of matrix $\mathbb{M}(C^k)$ are positive and all off-diagonal entries of $\mathbb{M}(C^k)$ are non-positive. The structure of edge-based matrices (27) implies that each column sum in $\mathbb{M}(C^k)$ is non-negative. Moreover, for elements having Dirichlet edges, the corresponding column sum is strictly positive. For a connected mesh, matrices $\mathbb{M}(C^k)$ and $\mathbb{M}^T(C^k)$ are irreducible since their directed graphs are strongly connected. Under the above conditions, the well-known linear algebra result [16] implies that matrix $\mathbb{M}^T(C^k)$ is the M -matrix and all entries of $(\mathbb{M}^T(C^k))^{-1}$ are positive. Since the inverse and transpose operations commute, $(\mathbb{M}^T(C^k))^{-1} = (\mathbb{M}^{-1}(C^k))^T$, we conclude that $\mathbb{M}(C^k)$ is monotone. Due to the signs of diagonal and off-diagonal entries $\mathbb{M}(C^k)$ is the M -matrix as well. Therefore, we proved the following theorem.

Theorem 4.1. Let $f \geq 0$, $g_D \geq 0$, $g_N \leq 0$ and $\Gamma_D \neq \emptyset$ in (1). If $C^0 \geq 0$ and linear systems in the Picard method are solved exactly, then $C^k \geq 0$ for $k \geq 1$.

5. Numerical experiments

We use discrete L_2 -norms to evaluate discretization errors for the concentration c and the flux \mathbf{q} :

$$\varepsilon_2^c = \left[\frac{\sum_{T \in \mathcal{T}} (c(\mathbf{x}_T) - C_T)^2 |T|}{\sum_{T \in \mathcal{T}} (c(\mathbf{x}_T))^2 |T|} \right]^{1/2} \quad \text{and} \quad \varepsilon_2^q = \left[\frac{\sum_{e \in \mathcal{E}_I \cup \mathcal{E}_B} ((\mathbf{q}_e - \mathbf{q}_e^h) \cdot \mathbf{n}_e)^2 |S_e|}{\sum_{e \in \mathcal{E}_I \cup \mathcal{E}_B} (\mathbf{q}_e \cdot \mathbf{n}_e)^2 |S_e|} \right]^{1/2},$$

where $|S_e|$ is a representative area for edge e . More precisely, $|S_e|$ is the arithmetic average of areas of mesh cells sharing the edge. The nonlinear iterations are terminated when the reduction of the initial residual norm becomes smaller than $\varepsilon_{non} = 10^{-9}$. The convergence tolerance for the linear solver is set to $\varepsilon_{lin} = 10^{-12}$.

5.1. Monotonicity test

5.1.1. Dirichlet boundary conditions

In this section, we verify numerically the assertion of Theorem 4.1. The problems with highly anisotropic diffusion tensor are challenging for any discretization method. Here we consider problem (1) defined in the unit square with a square hole, $\Omega = (0, 1)^2 / [4/9, 5/9]^2$. The boundary of Ω consists of two disjoint parts as shown in Fig. 2(a).

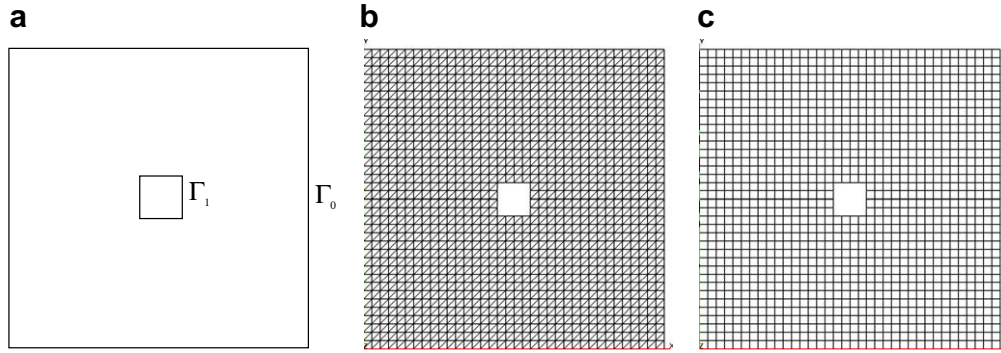


Fig. 2. (a) Sketch of the computational domain Ω . (b) Uniform triangular mesh. (c) Square mesh.

We set $\Gamma_N = \emptyset, f = 0, g_D = 0$ on $\Gamma_0, g_D = 2$ on Γ_1 , and take the anisotropic diffusion tensor \mathbb{K}

$$\mathbb{K} = R(-\theta) \begin{pmatrix} k_1 & 0 \\ 0 & k_2 \end{pmatrix} R(\theta), \quad R(\theta) = \begin{pmatrix} \cos \theta & \sin \theta \\ -\sin \theta & \cos \theta \end{pmatrix}, \tag{29}$$

where $k_1 = 100, k_2 = 1$ and $\theta = -\pi/6$.

According to the maximum principle for elliptic PDEs, the exact solution should be between 0 and 2. Let us consider the uniform triangular and quadrilateral meshes shown in Fig. 2(b) and (c). The solution calculated with the lowest-order Raviart–Thomas mixed finite element (MFE) method on the triangular mesh is shown in Fig. 3(a). In Fig. 3(b), we observe extensive areas where the discrete solution is negative. Solutions computed with the nonlinear FV method on triangular and square meshes are non-negative everywhere in Ω (see Fig. 4).

5.1.2. No-flow boundary conditions

Theorem 4.1 guarantees only non-negativity of the numerical solution. It means that in some situations the proposed method may violate the discrete maximum principle. In this subsection we investigate problems with homogeneous Neumann (no-flow) boundary conditions which frequently appear in simulations.

The problem, that we consider in this subsection, was also described and investigated in [3,17]. Let $\Omega = (0, 1)^2$ and \mathbb{K} be the anisotropic diffusion tensor:

$$\mathbb{K} = R(-\theta) \begin{pmatrix} k_1 & 0 \\ 0 & k_2 \end{pmatrix} R(\theta), \tag{30}$$

where $k_1 = 1, k_2 = 10^{-3}$ and $\theta = 67.5^\circ$.

The uniform 11×11 square partition \mathcal{T} is shown in Fig. 5(a). The source term $f(x, y)$ is set to zero. The scalar variable is fixed in two cells (4, 6) and (8, 6), representing the sink ($c = 0$) and the source ($c = 1$) terms, respectively. These terms result

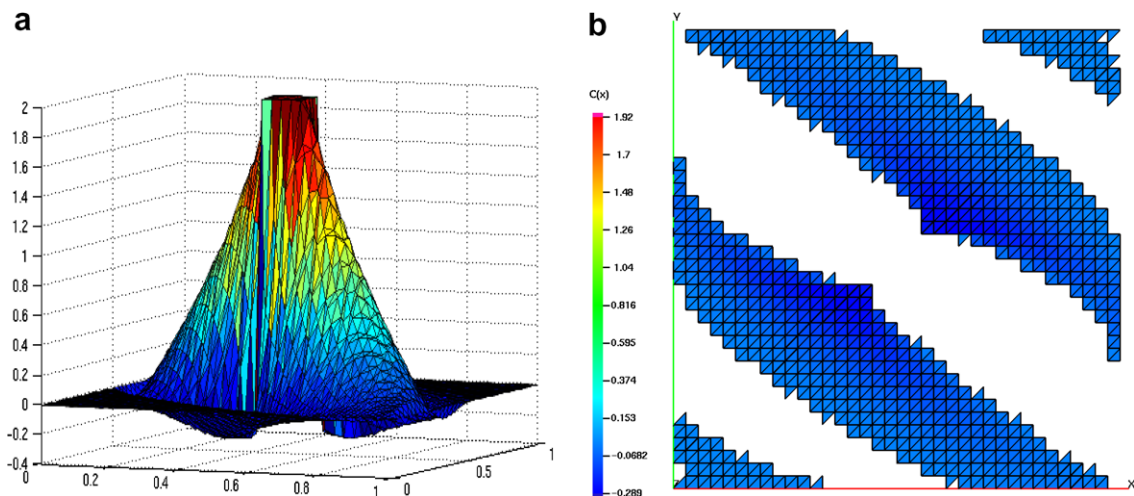


Fig. 3. (a) Solution calculated with the MFE method. (b) Part of Ω where this solution is negative.

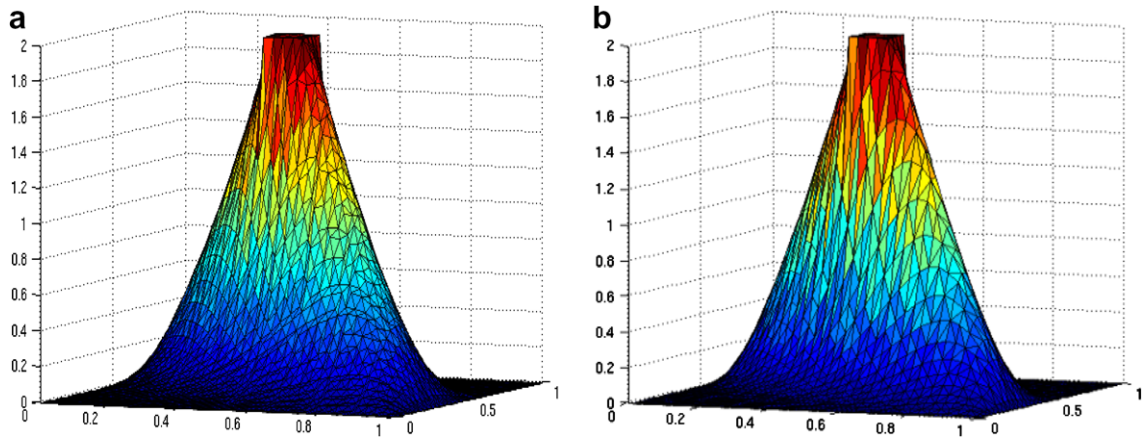


Fig. 4. Solutions calculated with the nonlinear FV method on triangular (a) and square (b) meshes.

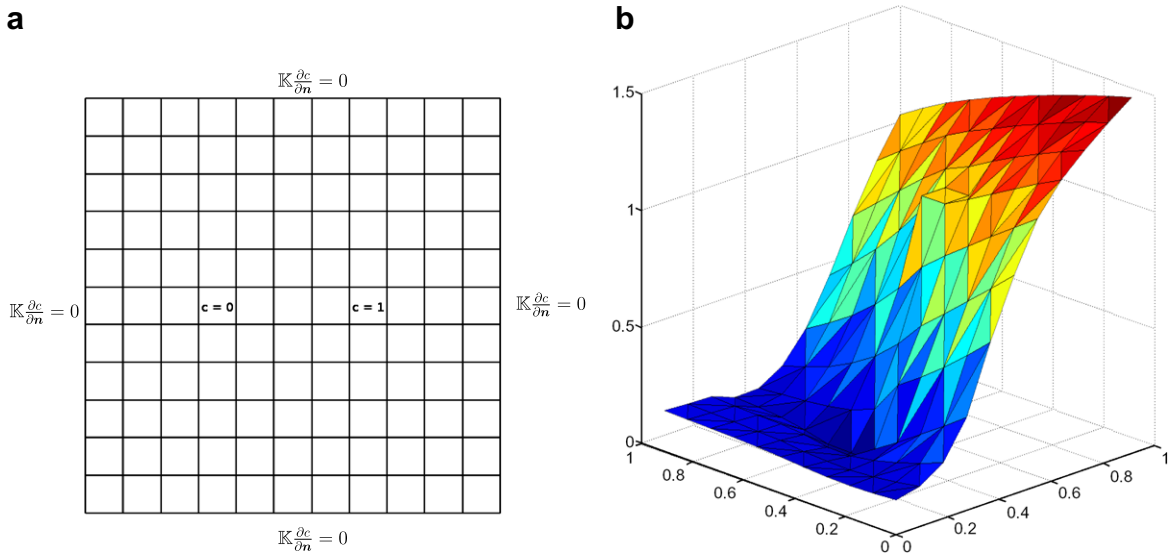


Fig. 5. The profile of numerical solution (b) calculated with the nonlinear FV method for the problem with no-flow boundary conditions on the uniform square mesh 11×11 (a).

in the Dirichlet boundary conditions on edges of these cells. The homogeneous Neumann boundary condition is set on the outer boundary:

$$\mathbb{K} \frac{\partial c}{\partial \mathbf{n}} = 0 \quad \text{on} \quad \partial\Omega.$$

The maximum principle for elliptic PDEs states that the exact solution should be between 0 and 1 and have no extrema on no-flow boundaries (the Hopf's second lemma). The numerical solution is shown in Fig. 5(b). In agreement with Theorem 4.1, the numerical solution is non-negative; however, some overshoots near the no-flow boundaries are observed. These overshoots are decreased as we refine the mesh and disappear on sufficiently fine meshes.

5.2. Picard method

The major computational overhead in the nonlinear FV methods comes from solution of the nonlinear algebraic problem. Here, we study the Picard method that guarantees solution positivity on each iteration.

We consider the first problem described in the previous section and two triangular meshes with $h = 1/36$ and $h = 1/72$. In Fig. 6, the interpolation-free nonlinear FV method is compared with two nonlinear FV methods described in [9]. One of these two methods uses the linear interpolation algorithm, while the other employs the inverse distance weighting (IWD) algorithm. The initial guess is $C^0 = 1$ for all methods.

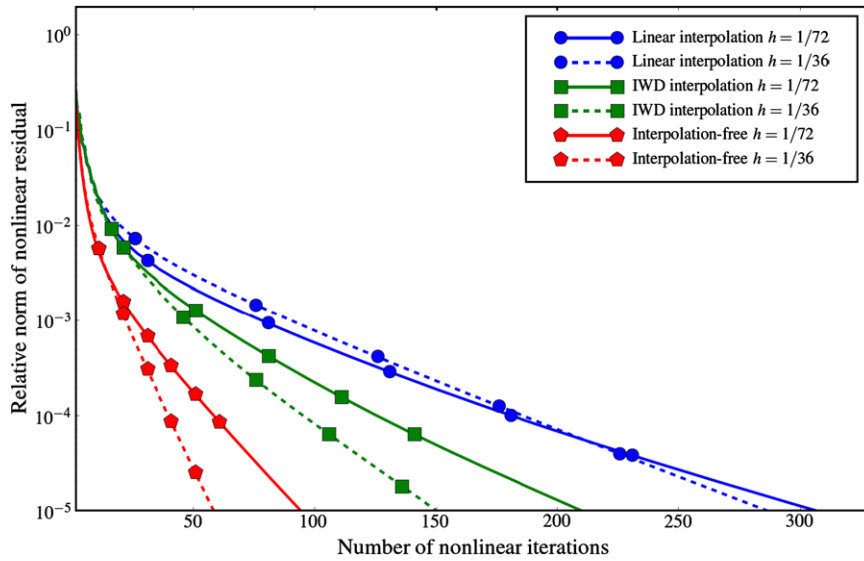


Fig. 6. Convergence of the Picard method for nonlinear FV methods with the linear interpolation (marked by circle), the inverse-weighted distance interpolation (marked by squares) and without interpolation (marked by pentagons). The solid line correspond to 72×72 mesh. The dashed lines correspond to 36×36 mesh.

All methods show fast convergence during the first 10–15 Picard iterations and then slow down. The results indicate that the convergence rate depends on the mesh resolution. The interpolation-free method is the fastest one. We observed similar behavior in many other experiments where the computational mesh was not aligned with the solution. The IWD interpolation method is more preferable for solutions with sharp gradients [9]. This may explain why its convergence is faster compared to the method with linear interpolation.

Next, we study convergence of nonlinear iterations for the second problem described in the previous section. Again, we compare the interpolation-free nonlinear FV method with the two nonlinear FV methods described in [9]. In Fig. 7 the number of iterations required to reduce the nonlinear residual in 10^5 times is plotted as a function of the mesh step size h . On coarse meshes the methods using the interpolation techniques converge faster. However, on finer meshes the interpolation-free method requires much less iterations. Moreover, this difference in the number of nonlinear iterations grows as the mesh

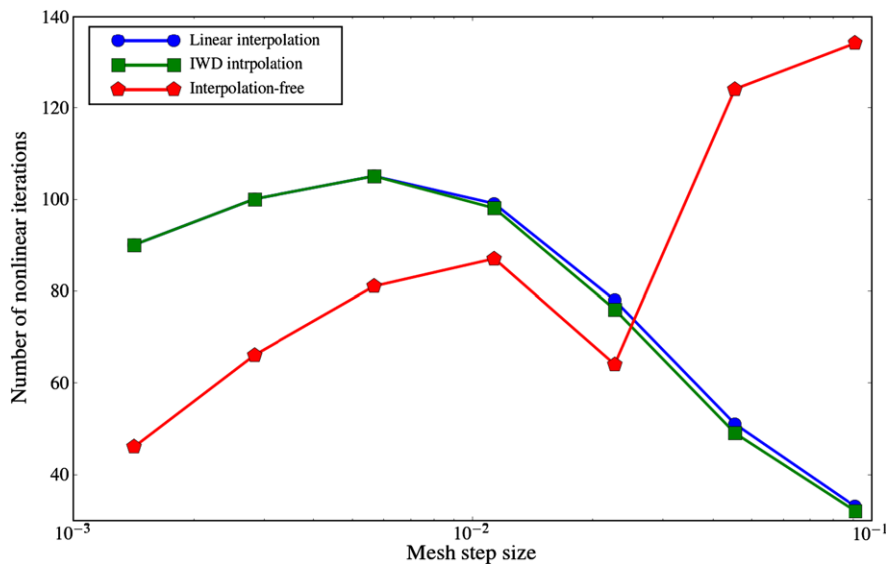


Fig. 7. The number of Picard iterations required to reduced the nonlinear residual 10^5 times as a function of the mesh step size h . The nonlinear FV methods with linear interpolation (marked by circles) and inverse-weighted distance interpolation (marked by squares) are compared with the FV method without interpolation (marked by pentagons).

refined. It may be caused by the step-like shape of the solution. As soon as the steepest part of the solution is well resolved, the nonlinear method converges faster.

The Newton-type methods, such as the Newton–Raphson method, can be considered for reducing the number of nonlinear iterations. However, a few issues have to be resolved before employing them. These methods do not guarantee solution positivity after each iteration. The lack of positivity may result in division by zero in (16). Imposing of some positivity constraints may result in deterioration of their convergence properties. Analysis of these methods will be the direction for future research and is beyond the scope of this paper.

5.3. Convergence study: smooth solution

In this section we investigate the convergence of the method for problems with a smooth solution. Let $\Omega = (0, 1)^2$

$$c(x, y) = \frac{1}{2\pi^2} \sin(\pi x) \sin(\pi y) \quad \text{and} \quad \mathbb{K} = \begin{pmatrix} 1 & 0 \\ 0 & 100 \end{pmatrix} \quad (31)$$

be the exact solution and the anisotropic diffusion tensor, respectively.

The convergence study is performed on three sequences of distorted triangular, distorted quadrilateral and polygonal meshes. The distorted mesh is constructed from the uniform mesh with the mesh size h by random distortion of internal nodes (x, y) :

$$x := x + \alpha \xi_x h, \quad y := y + \alpha \xi_y h, \quad (32)$$

where ξ_x and ξ_y are random variables with values between -0.5 and 0.5 and $\alpha \in [0, 1]$ is the degree of distortion. To avoid mesh tangling, we set $\alpha = 0.4$ for triangular meshes and $\alpha = 0.7$ for quadrilateral meshes. It is pertinent to emphasize that the distortion is performed on each refinement level. Examples of these meshes are shown in Fig. 8. For each space resolution, the quadrilateral and polygonal meshes have roughly the same number of cells. The corresponding triangular meshes have twice more cells.

The presented FV method is exact for piecewise-linear concentrations, so we may expect the second-order of convergence for the scalar variable C and at least the first-order of convergence for the flux degrees of freedom. The convergence results are presented in Table 1. The convergence rate for the scalar variable C increases as the meshes are refined and tends to the asymptotic second-order. For the normal component of the flux, the convergence rate is higher than the first-order in all cases: on randomly distorted meshes (triangular and quadrilateral meshes) and on smooth meshes (polygonal meshes).

In the next group of tests we study the problem with an isotropic and homogeneous diffusion tensor defined on highly anisotropic meshes. The particular example is described in [3] where the authors demonstrate that for this type of problems

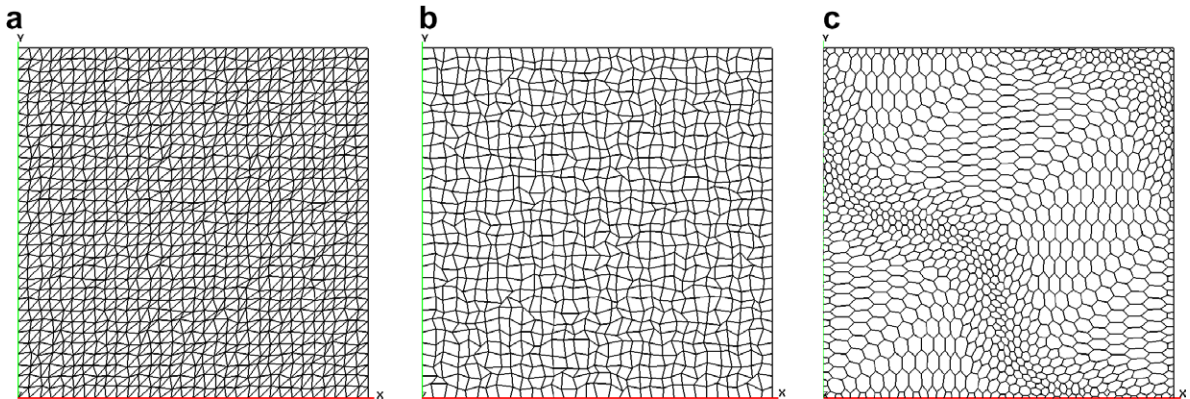


Fig. 8. Examples of distorted triangular (a), distorted quadrilateral (b) and polygonal (c) meshes.

Table 1

The convergence results for the problem with the smooth solution (31).

h	Triangular meshes		Quadrilateral meshes		Polygonal meshes	
	ε_2^c	ε_2^q	ε_2^c	ε_2^q	ε_2^c	ε_2^q
1/16	1.20e-02	1.95e-02	8.47e-03	2.15e-02	1.59e-02	3.99e-02
1/32	4.74e-03	8.71e-03	2.34e-03	1.03e-02	5.86e-03	1.35e-02
1/64	1.65e-03	3.62e-03	6.64e-04	4.25e-03	1.80e-03	4.68e-03
1/128	5.20e-04	1.38e-03	2.06e-04	1.78e-03	4.67e-04	1.63e-03
1/256	1.50e-04	5.38e-04	5.89e-05	7.85e-04	1.10e-04	6.01e-04

the convergence of MPFA $O(\eta)$ -methods is lost. Following the description of numerical tests presented in [3], we consider distorted and undistorted parallelogram meshes with different aspect ratios, 0.1 and 0.01 (see Fig. 9). The distorted meshes are constructed using a modified formula (32) with different mesh steps h_x and h_y .

Let $c(x, y) = \cosh(\pi x) \cos(\pi y)$ be the exact solution of the problem at hand. We consider a homogeneous isotropic medium and zero source term. The convergence results are presented in Table 2. For both aspect ratios, the second-order convergence for the scalar variable is observed. Convergence for the flux variable is the second-order on undistorted meshes and reduces to the first-order on distorted meshes.

5.4. Convergence study: solutions with sharp gradients

In the next set of numerical experiments, we study convergence of the nonlinear FV method for a problem with a known highly anisotropic solution. We consider problem (1) defined in the unit square $\Omega = (0, 1)^2$ which is divided into three sub-domains $\Omega_1 = (0, 1) \times (0, Y_1), \Omega_2 = (0, 1) \times [Y_1, Y_2], \Omega_3 = (0, 1) \times (Y_2, 1)$ as shown in Fig. 10(a). We impose the homogeneous Dirichlet boundary condition on $\partial\Omega$ and set the source function and the diffusion tensor as follows:

$$f(x, y) = \begin{cases} 0, & (x, y) \in \Omega_1 \cup \Omega_3, \\ f_0(y)\sin(\pi x) & (x, y) \in \Omega_2, \end{cases} \quad \mathbb{K} = \begin{pmatrix} k_1 & 0 \\ 0 & 1 \end{pmatrix}.$$

In our experiments $f_0(y) = 100, k_1 = 100, Y_1 = 3/8$ and $Y_2 = 5/8$. The exact solution to this problem can be calculated using the separation of variables. Taking

$$C(x, y) = \phi(y)\sin(\pi x)$$

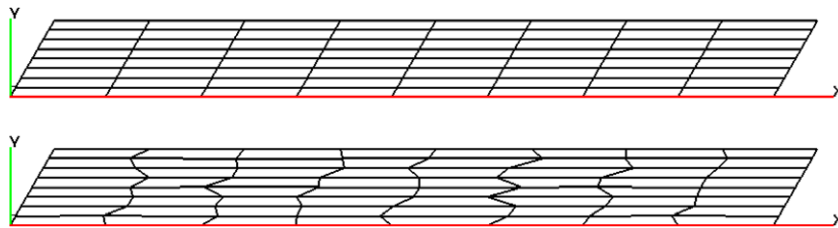


Fig. 9. Parallelogram meshes with aspect ratio 0.1. Angle 30°. Above: undistorted. Below: distorted.

Table 2

The convergence results for the problem defined on the anisotropic parallelogram meshes.

h	Undistorted meshes				Distorted meshes			
	Aspect ratio 0.1		Aspect ratio 0.01		Aspect ratio 0.1		Aspect ratio 0.01	
	ϵ_2^c	ϵ_2^q	ϵ_2^c	ϵ_2^q	ϵ_2^c	ϵ_2^q	ϵ_2^c	ϵ_2^q
1/16	1.54e-03	6.08e-02	3.02e-03	2.49e-01	1.93e-03	7.96e-02	3.16e-03	6.40e-01
1/32	2.71e-04	1.79e-02	5.47e-04	5.74e-02	3.38e-04	2.28e-02	5.28e-04	2.30e-01
1/64	6.56e-05	5.01e-03	8.98e-05	1.42e-02	9.70e-05	1.23e-02	1.18e-04	1.28e-01
1/128	1.65e-05	1.40e-03	1.23e-05	3.75e-03	2.72e-05	5.21e-03	4.06e-05	7.34e-01

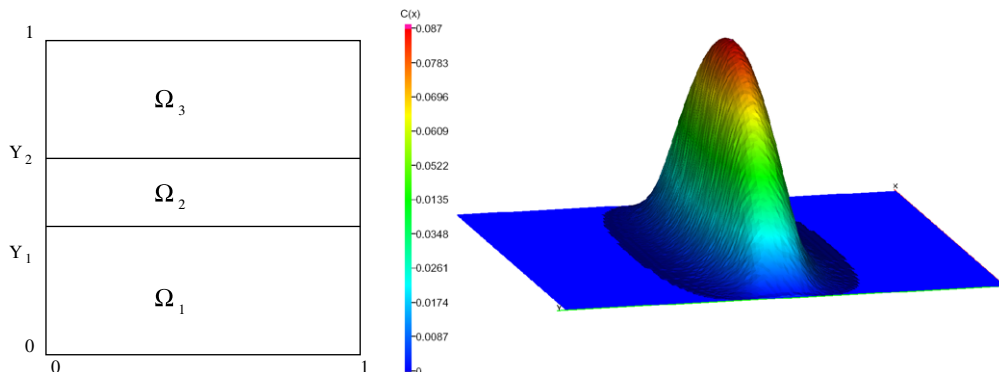


Fig. 10. (a) The computational domain for the problem defined in Section 5.4. (b) The discrete solution calculated with the nonlinear FV method.

and substituting it into equation (1), we get the following equation for $\phi(y)$:

$$-\frac{\partial^2 \phi}{\partial y^2} + \pi^2 k_1 \phi(y) = \hat{f}(y) \quad \text{where} \quad \hat{f}(y) = \begin{cases} 0, & y \in [0, Y_1] \cup [Y_2, 1] \\ f_0(y) & y \in (Y_1, Y_2) \end{cases}$$

that can be solved analytically. We seek the solution in the form

$$\phi(y) = a \exp(\pi\sqrt{k_1}y) + b \exp(-\pi\sqrt{k_1}y) + \frac{1}{\pi^2 k_1} \hat{f}(y),$$

where coefficients a and b are constant on each of the three intervals. The continuity and boundary conditions result in a 6×6 system for these coefficients. The solution $C(x, y)$ is shown in Fig. 10(b).

The numerical tests were performed on the meshes defined in Section 5.3 with the same order of distortion. The vertices located on lines $y = Y_1$ and $y = Y_2$ were distorted only in the x -direction. The polygonal meshes were modified slightly to conform to these lines. Each polygonal cell intersected by one of these lines was split into two cells.

The computed errors are collected in Table 3. Due to high order of the mesh distortion and large solution gradients (see Fig. 10(b)), we observe slow convergence for the scalar unknown C on the coarse meshes. On the fine meshes, $h = 1/128, 1/256$, the convergence rate increases and becomes close to the second-order for triangular and quadrilateral meshes. For polygonal meshes, the convergence rate grows but does not yet reach the asymptotic rate on the finest mesh. The way we adapt the polygonal meshes to lines $y = Y_1$ and $y = Y_2$ results in strong dis-proportionality of neighboring mesh cells. This may be one of the reasons for slowing down the convergence rate. The flux variable \mathbf{q}^h converges with the first-order on all meshes.

5.5. Convergence study: discontinuous diffusion tensor

In this section we investigate convergence of our method for a problem with a heterogeneous diffusion tensor. Let Ω be the unit square and \mathbb{K} changes the eigenvalues and orientation of eigenvectors across the line $x = 0.5$. Let $\mathbb{K}(\mathbf{x}) = \mathbb{K}^{(1)}$ for $x \leq 0.5$ and $\mathbb{K}(\mathbf{x}) = \mathbb{K}^{(2)}$ otherwise, where

Table 3

The convergence results for the problem with the anisotropic solution defined in Section 5.4.

h	Triangular meshes		Quadrilateral meshes		Polygonal meshes	
	\mathcal{E}_2^C	\mathcal{E}_2^q	\mathcal{E}_2^C	\mathcal{E}_2^q	\mathcal{E}_2^C	\mathcal{E}_2^q
1/16	1.21e-01	1.68e-01	8.28e-02	1.71e-01	7.01e-02	1.96e-01
1/32	1.02e-01	1.41e-01	4.93e-02	8.21e-02	6.20e-02	1.09e-01
1/64	5.81e-02	7.85e-02	2.43e-02	3.97e-02	3.79e-02	6.18e-02
1/128	2.20e-02	3.49e-02	7.91e-03	1.86e-02	1.57e-02	2.68e-02
1/256	6.08e-03	1.54e-02	1.94e-03	8.81e-03	5.32e-03	8.55e-03

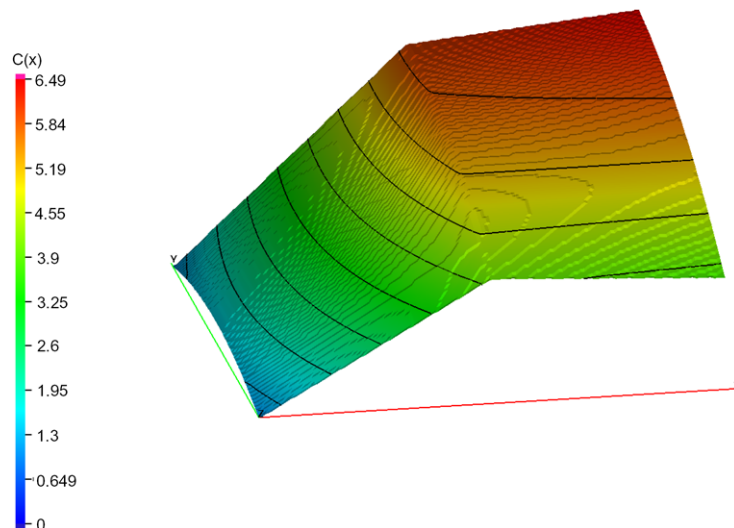


Fig. 11. The solution profile for the problem with the heterogeneous diffusion tensor.

Table 4

The convergence results for the problem with the heterogeneous diffusion tensor.

h	Triangular meshes		Quadrilateral meshes		Polygonal meshes	
	\mathcal{E}_2^c	\mathcal{E}_2^q	\mathcal{E}_2^c	\mathcal{E}_2^q	\mathcal{E}_2^c	\mathcal{E}_2^q
1/16	2.92e–04	7.38e–03	3.71e–04	1.02e–02	4.55e–04	1.08e–02
1/32	7.56e–05	2.97e–03	1.04e–04	4.61e–03	1.25e–04	3.33e–03
1/64	2.12e–05	1.18e–03	2.31e–05	1.96e–03	3.45e–05	1.11e–03
1/128	5.41e–06	4.83e–04	6.70e–06	8.92e–04	9.03e–06	3.92e–04
1/256	1.38e–06	2.08e–04	1.64e–06	4.14e–04	2.35e–06	1.40e–04

$$\mathbb{K}^{(1)} = \begin{pmatrix} 1 & 0 \\ 0 & 1 \end{pmatrix} \quad \text{and} \quad \mathbb{K}^{(2)} = \begin{pmatrix} 10 & 3 \\ 3 & 1 \end{pmatrix}.$$

Note that $\text{cond}(\mathbb{K}^{(1)}) = 1$ and $\text{cond}(\mathbb{K}^{(2)}) = 118.99$. We choose the following exact solution:

$$c(x, y) = \begin{cases} 1 - 2y^2 + 4xy + 2y + 6x & \text{if } x \leq 0.5, \\ b_2y^2 + c_2xy + d_2x + e_2y + f_2 & \text{if } x > 0.5, \end{cases}$$

where

$$b_2 = -2, \quad c_2 = \frac{4\mathbb{K}_{11}^{(2)} - 2\mathbb{K}_{12}^{(2)} - 2}{\mathbb{K}_{11}^{(2)}}, \quad d_2 = \frac{4(\mathbb{K}_{12}^{(2)} + 1)}{\mathbb{K}_{11}^{(2)}}, \quad f_2 = \frac{4\mathbb{K}_{11}^{(2)} + 2\mathbb{K}_{12}^{(2)} - 3}{\mathbb{K}_{11}^{(2)}}.$$

The numerical tests were performed on distorted triangular, distorted quadrilateral and polygonal meshes. The order of distortion is the same as in the previous sections. The mesh nodes located on the line $x = 0.5$ were distorted only in the y -direction. The polygonal meshes were modified as before to conform to this line. The solution profile is shown in Fig. 11. The convergence results presented in Table 4 demonstrate that the heterogeneity of the diffusion tensor does not affect the convergence rate for all the considered meshes.

6. Conclusion

We developed and analyzed the new monotone finite volume method for anisotropic diffusion equation. We have proved that this method guarantees nonnegativity of the numerical solution if the source term and the initial guess are non-negative. The distinctive feature of the proposed method is that no interpolation technique is employed. This provides more robust and faster convergence of nonlinear iterations in comparison with the methods described in [9]. The method is applicable to polygonal meshes and full anisotropic heterogeneous diffusion tensors. The numerical experiments demonstrate the second-order convergence for the scalar unknown and the first-order convergence for the flux variable (a) on meshes with small aspect ratios and (b) for problems with highly anisotropic coefficients.

The future research direction is the reduction of the computational cost of solving the nonlinear algebraic problem by using more efficient iterative methods. Another open problem is conforming the discrete maximum principle. A new approach to this problem was proposed recently by Potier [11].

Acknowledgments

This work was carried out under the auspices of the National Nuclear Security Administration of the US Department of Energy at Los Alamos National Laboratory under Contract No. DE-AC52-06NA25396 and the DOE Office of Science Advanced Scientific Computing Research (ASCR) Program in Applied Mathematics Research.

The authors thank Dr. M. Shashkov (LANL) for fruitful discussions on the paper topic and many useful comments. The authors are also grateful to Prof. Yu. Kuznetsov (University of Houston) for proposing the test case studied in Section 5.4.

References

- [1] J. Martin-Herrero, Anisotropic diffusion in the hypercube, IEEE T. Geosci. Remote. 45 (5) (2007) 1386–1398.
- [2] J.M. Nordbotten, I. Aavatsmark, G.T. Eigestad, Monotonicity of control volume methods, Numer. Math. 106 (2) (2007) 255–288.
- [3] I. Aavatsmark, G. Eigestad, B. Mallison, J. Nordbotten, A compact multipoint flux approximation method with improved robustness, Numer. Meth. Part. D. E. 24 (5) (2008) 1329–1360.
- [4] P.G. Ciarlet, P.-A. Raviart, Maximum principle and uniform convergence for the finite element method, Comput. Methods Appl. Mech. Eng. 2 (1973) 17–31.
- [5] V. Ruas Santos, On the strong maximum principle for some piecewise linear finite element approximate problems of nonpositive type, J. Fac. Sci. Univ. Tokyo Sect. IA Math. 29 (2) (1982) 473–491.
- [6] S. Korotov, M. Křížek, P. Neittaanmäki, Weakened acute type condition for tetrahedral triangulations and the discrete maximum principle, Math. Comp. 70 (233) (2001) 107–119 (electronic).
- [7] E. Burman, A. Ern, Discrete maximum principle for Galerkin approximations of the laplace operator on arbitrary meshes, C. R. Math. Acad. Sci. Paris 338 (8) (2004) 641–646.

- [8] C. LePotier, Schema volumes finis monotone pour des operateurs de diffusion fortement anisotropes sur des maillages de triangle non structures, C. R. Math. Acad. Sci. Paris 341 (2005) 787–792.
- [9] K. Lipnikov, D. Svyatskiy, M. Shashkov, Y. Vassilevski, Monotone finite volume schemes for diffusion equations on unstructured triangular and shape-regular polygonal meshes, J. Comp. Phys. 227 (2007) 492–512.
- [10] A. Yuan, Z. Sheng, Monotone finite volume schemes for diffusion equation polygonal meshes, J. Comp. Phys. 227 (2008) 6288–6312.
- [11] C.L. Potier, Finite volume scheme satisfying maximum and minimum principles for anisotropic diffusion operators, in: R. Eymard, J.-M. Herard (Eds.), Finite Volumes for Complex Applications V, 2008, pp. 103–118.
- [12] I. Kapyrin, A family of monotone methods for the numerical solution of three-dimensional diffusion problems on unstructured tetrahedral meshes, Dokl. Math. 76 (2) (2007) 734–738.
- [13] Y. Vassilevski, I. Kapyrin, Two splitting schemes for nonstationary convection–diffusion problems on tetrahedral meshes, Comput. Math. Math. Phys. 48 (8) (2008) 1349–1366.
- [14] H. van der Vorst, Bi-CGSTAB: a fast and smoothly converging variant of Bi-CG for the solution of non-symmetric linear systems, SIAM J. Sci. Stat. Comput. 13 (2) (1992) 631–644.
- [15] I.E. Kaporin, High quality preconditioning of a general symmetric positive definite matrix based on its $u^t u + u^t r + r^t u$ -decomposition, Numer. Linear Algebra Appl. 5 (6) (1998) 483–509.
- [16] R.S. Varga, Matrix iterative analysis, Prentice-Hall Inc., Englewood Cliffs, NJ, 1962.
- [17] D. Svyatskiy, Nonlinear monotone finite volume method, in: R. Eymard, J.-M. Herard (Eds.), Finite Volumes for Complex Applications V, 2008, pp. 935–947.